

Scaling and phase diagrams of planetary sediment transport

Thomas Pähzt,^{1*} Orencio Durán,² Francesco Comola³

¹Institute of Port, Coastal and Offshore Engineering, Ocean College, Zhejiang University, 310058 Hangzhou, China

²Department of Ocean Engineering, Texas A&M University, College Station, Texas 77843-3136, USA

³Department of Atmospheric and Oceanic Sciences, University of California, Los Angeles, CA 90095, USA

*To whom correspondence should be addressed; E-mail: tpaehzt@gmail.com.

Sediment transport by atmospheric winds shapes the surface and affects the climates of planetary bodies. Reliably predicting the occurrence and rate of sediment transport in the Solar System has been notoriously difficult because fluid density, grain size and soil cohesiveness vary across many orders of magnitude. Here, we use recent advances in analytical and numerical sediment transport modeling to derive general scaling relations for planetary transport. In particular, we show that the equations of motion of rebounding grains predict that the minimum threshold fluid shear velocity needed to sustain transport (transport cessation threshold) scales with the particle-fluid-density ratio (s) as $s^{1/3}$, in contrast to the $s^{1/2}$ -scaling exhibited by the threshold for transport initiation. The grain size corresponding to this minimum is in the range 80–290 μm for Solar System bodies. Our results, summarized in phase di-

ograms for the cessation threshold, mean transport rate and dust emission potential, explain the observed eastward propagation of Titan's dunes, in spite of a predominantly westward wind circulation, indicate active dust cycles on Earth, Mars and Titan, and suggest marginal but active atmospheric transport on Venus, Triton and Pluto.

Introduction

Aeolian (wind-driven) transport of nonsuspended grains, including sand, ice and snow, is an ubiquitous phenomenon that leads to a rich variety of multiscale surface features on Earth and other planetary bodies (1–5). As suggested by the presence of wind streaks and dunes, it may even occur in the very rarefied atmospheres of Neptune's moon Triton (6), Pluto (7) and the comet 67P/Churyumov-Gerasimenko (8). Aeolian transport also affects planetary bodies' climates via the emission of soil dust into their atmospheres, predominantly caused by the bombardment of the soil by moving sand grains (2). Driven by fluid drag and gravity, most transported sand-sized and larger grains regularly interact with the bed surface as flow turbulence is too weak to suspend them. For denser fluids, like water and most liquids, this near-surface grain motion occurs in the form of rolling, sliding and small hops (*bedload*), while for lighter fluids, like most gases, grains move in more energetic hops (*saltation*). Until recently, a physical description of the entrainment of bed sediment into the transport layer, caused by impacts of saltating grains, was considered an essential ingredient of any realistic model predicting the equilibrium transport rate of aeolian saltation (9, 10) and its cessation threshold (11, 12) (i.e., the flow speed below which saltation ceases). If this were the case, reliable predictions of extraterrestrial aeolian transport rates would be very difficult to provide, since the susceptibility of bed sediment to such impact entrainment decreases with the cohesiveness of the bed material (13) and the cohesiveness of extraterrestrial soils is very challenging to estimate accurately (e.g.,

existing estimations of the cohesiveness of the surface material of Titan vary by several orders of magnitude (14, 15)).

Recent numerical simulations of aeolian saltation (13), supported by simplified models and theoretical analysis (16), suggest that soil cohesiveness, although it strongly decreases the rate of impact entrainment, barely affects the equilibrium transport rate and cessation threshold. A possible explanation is that the statistical properties of saltation are largely controlled by the energy balance of transported grains—where the energy gained by fluid drag equals the energy dissipated by collisions—which is independent on impact entrainment (16–20). This finding suggests that cohesion can be neglected in a first approximation of the physical description of the equilibrium properties of saltation, simplifying the theoretical analysis and opening the way to the derivation of general scaling relations and the development of simplified models.

Here, we combine existing numerical (21) and analytical (16–19) models of aeolian and subaqueous transport of cohesionless nonsuspended sediments (Materials and Methods) with new analytical derivations to describe transport modes, cessation thresholds, equilibrium transport rates and dust emission potential across planetary conditions. The numerical model (21) resolves both grain-grain and fluid-grain interactions and the resulting change in the average flow field, and successfully reproduces subaqueous and aeolian transport (18, 19) (Materials and Methods). Numerical simulations overcome a common problem with wind tunnel experiments of extraterrestrial aeolian transport: they lack sufficient feeding of sediment at the leading edge of the bed (22–29), which is required for sustaining equilibrium transport conditions near the cessation threshold because of the limited fetch of such wind tunnels. In that regard, the simulations capture natural field conditions, where long fetches, along with a variety of mechanisms to generate airborne grains, can plausibly lead to equilibrium transport near the cessation threshold (7, 17, 30) (see Supplementary Materials for details).

We perform transport simulations for a wide range of planetary conditions to test analytically-

derived scaling relations for the transport cessation threshold, and validate an analytical model (16) that predicts the cessation threshold curves and estimates the dominant transport regime, whether bedload, saltation or suspension, close to the threshold. The results from this analytical model (called here the “cessation threshold model”) are then used to parametrize both an existing analytical formulation for the equilibrium transport rate (19) and a new formulation for the impact kinetic energy flux (Materials and Methods), and subsequently generate predictions of the sediment transport potential and impact-driven dust emission potential, respectively, for arbitrary planetary conditions.

Relevant parameters for planetary sediment transport. The average properties of equilibrium sediment transport are mainly determined by a few grain and environmental parameters: grain and fluid densities (ρ_p and ρ_f , respectively), median grain diameter (d), fluid dynamic viscosity (μ), fluid shear velocity (u_*) and gravitational constant (g), or its buoyancy-reduced value $\tilde{g} \equiv (1 - \rho_f/\rho_p)g$ (for air, $\tilde{g} \simeq g$). Typically, these parameters are combined into three dimensionless numbers (18, 19): the particle-fluid-density ratio $s \equiv \rho_p/\rho_f$, Galileo number $Ga \equiv \rho_f \sqrt{s\tilde{g}d^3}/\mu$ and Shields number $\Theta \equiv u_*^2/(s\tilde{g}d)$. However, since the most important parameter for planetary transport is the fluid density ρ_f , which varies by several orders of magnitude across atmospheres on Solar System bodies (Tables S1 and S2), a more convenient phase space for planetary transport would ideally isolate the density ratio s from the other dimensionless numbers. Therefore, we replace the Galileo number, which is essentially a rescaled grain size to the power 3/2 and depends strongly on ρ_f , by a new rescaled grain size $d^+ = d/d_\mu$ independent on ρ_f , with d_μ defined as $d_\mu \equiv [\mu/(\rho_p \sqrt{\tilde{g}})]^{2/3}$. Similarly, we replace the Shields number by the rescaled fluid shear velocity $u_*^+ = u_*/\sqrt{\tilde{g}d_\mu}$. The characteristic diameter d_μ has the additional advantage that it is remarkably insensitive to aeolian transport conditions across Solar System bodies, varying by only a factor of 2, between 1.53 μm on Mars and 3.08 μm on

Pluto (Table S2).

In rarefied (low-fluid density) atmospheres, sediment transport is also affected by the Mach number (the ratio of the relative fluid velocity to the speed of sound c), which reduces the drag coefficient at the typically low Reynolds numbers characterizing transport in rarefied conditions (31) (Materials and Methods). The importance of rarefaction effects is characterized by the Knudsen number Kn , defined as the ratio of the mean free path of fluid molecules λ to the grain size d , and given by $Kn = \sqrt{k\pi/2}\mu/(\rho_f c d)$, where k is the adiabatic exponent. Using dimensionless numbers and introducing the rescaled speed of sound $c^+ = c/\sqrt{\tilde{g}d_\mu}$, the Knudsen number becomes $Kn = 1.48 s/(c^+ d^+)$ for diatomic gases ($k = 1.4$). Interestingly, the rescaled speed of sound, $c^+ \approx 9 \times 10^4$, varies by less than 10% across atmospheres on Solar System bodies (Table S2).

The phase space of equilibrium planetary transport is thus completely determined by four independent numbers: s , d^+ , u_*^+ and c^+ , representing the particle-fluid-density ratio and rescaled grain size, fluid shear stress and speed of sound, respectively.

Results

Scaling of the cessation threshold for saltation. Sediment transport can be sustained by the fluid only when the rescaled fluid shear velocity u_*^+ exceeds the cessation threshold $u_{*t}^+ = u_{*t}/\sqrt{\tilde{g}d_\mu}$, which is function of the remaining parameters s , d^+ and c^+ . For saltation, the dominant aeolian transport mode (see Materials and Methods and Fig. S1 for distinction between transport modes), numerical simulations of planetary transport reveal a lower bound for $u_{*t}^+(s, d^+)$ scaling as $s^{1/3}$ (Fig. 1(a), filled symbols). This is distinct from the classical scaling of the saltation initiation threshold with $s^{1/2}$ measured in wind tunnel experiments (22–28) (Fig. 1(a), pluses) that follows from a balance between flow-induced and resisting forces or torques acting in bed surface grains (17). In contrast to transport initiation, during transport

cessation, saltating grains are essentially moving in (quasi)periodic trajectories extracting just enough energy from the flow to balance the energy dissipated during bed rebounds (18). This energy dissipation is characterized by scale-free boundary condition linking the distribution of impact grain velocities to the distribution of rebound or lift-off grain velocities, without the introduction of any resisting force at the bed (32).

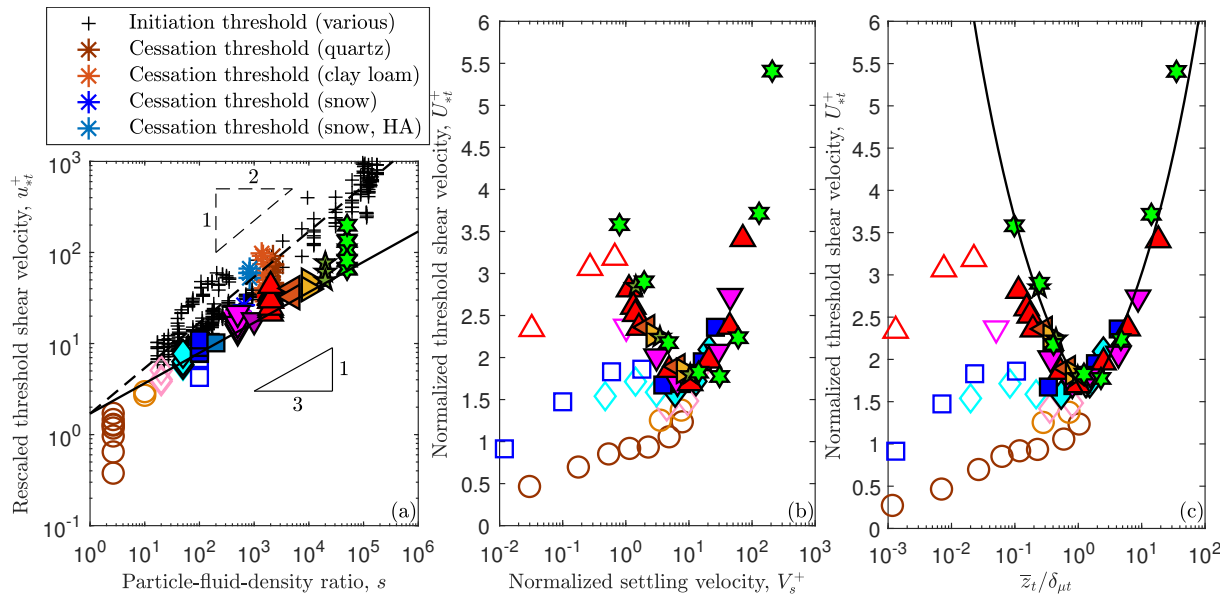


Figure 1: Lower bound of saltation cessation threshold. (a) Rescaled threshold shear velocity $u_{*t}^+ = u_{*t} / \sqrt{\tilde{g}d_\mu}$ versus density ratio $s \equiv \rho_p / \rho_f$. (b) normalized threshold shear velocity $U_{*t}^+ = s^{-1/3} u_{*t}^+$ versus normalized settling velocity $V_s^+ = s^{-1/3} v_s^+$, with $v_s^+ = v_s / \sqrt{\tilde{g}d_\mu}$. (c) U_{*t}^+ versus the transport layer thickness \bar{z}_t to viscous sublayer thickness $\delta_{\mu t}$ ratio at the threshold. Symbols that appear in the legend of (a) correspond to cessation (33–38) and initiation (22–28) threshold measurements. Symbols that do not appear in the legend of (a) correspond to numerical simulations for various combinations of $s \in [2.65, 5 \times 10^4]$ and the rescaled grain size $d^+ = d / d_\mu$, with open and filled symbols indicating bedload and saltation conditions, respectively (see Fig. S1 for simulation phase space). The solid line in (a) corresponds to $u_{*t}^+ \propto s^{1/3}$ and represents the lower bound for cessation and initiation thresholds of saltation. The solid lines in (c) corresponds to the analytical prediction $U_{*t}^+ \propto (\bar{z}_t / \delta_{\mu t})^\beta$, with $\beta = -1/3$ (left branch) and $\beta = 1/3$ (right branch).

The scaling of the cessation threshold with $s^{1/3}$ arises from the form of the equations of motion of a saltating grain moving in a periodic trajectory within the inner turbulent boundary

layer (Materials and Methods). Considering in a first approximation only hydrodynamically smooth saltation, the rescaled impact velocity \hat{v}_\downarrow of a saltating grain rebounding with a lift-off velocity \hat{v}_\uparrow (where both velocities are rescaled by the settling velocity v_s) has the general form $\hat{v}_\downarrow = f(\hat{v}_\uparrow|U_*^+, V_s^+)$, where the dependence on the transport parameters s , d^+ , u_*^+ and c^+ is hidden within the normalized shear velocity $U_*^+ = s^{-1/3}u_*^+$ and normalized settling velocity $V_s^+ = s^{-1/3}v_s^+$, with rescaled settling velocity $v_s^+(s, d^+, c^+) = v_s/\sqrt{\tilde{g}d_\mu}$ (Materials and Methods). Combining this relation with a scale-free rebound condition and an additional constraint at the cessation threshold, it follows that $U_*^+ = U_{*t}^+$ is a function of only V_s^+ for saltation (Materials and Methods).

The relation between the normalized threshold shear velocity $U_{*t}^+ = s^{-1/3}u_{*t}^+$ and normalized settling velocity V_s^+ is confirmed by numerical simulations of saltation (Fig. 1(b)), where the minimum corresponds exactly to the lower bound $u_{*t}^+ \propto s^{1/3}$ in Fig. 1(a).

Hydrodynamic origin of the minimum of the cessation threshold for saltation and the most mobile grain size. The minimum of U_{*t}^+ occurs when the transport layer thickness \bar{z}_t at the threshold is about equal to the viscous sublayer thickness at the threshold $\delta_{\mu t} = 10\mu/(\rho_f u_{*t}) = 10sd_\mu/u_{*t}^+$ (Fig. 1(c)). As explained in the Materials and Methods, this is related to the change in the scaling of the flow velocity with elevation across the viscous sublayer (from linear to logarithmic) and the fact that the average flow velocity is related to the average grain vertical velocity (Fig. S2), their hop height and thus the transport layer thickness (Fig. S1(a)). These relations predict a power-law scaling $U_{*t}^+ \propto (\bar{z}_t/\delta_{\mu t})^\beta$, with an exponent β that changes abruptly from $-1/3$ for “viscous saltation” ($\bar{z}_t/\delta_{\mu t} < 1$) to $1/3$ for “turbulent saltation” ($\bar{z}_t/\delta_{\mu t} > 1$) (Fig. 1(c)).

We can use the functional relation $U_{*t}^+(V_s^+)$ for saltation (Fig. 1(b)) to obtain the first-order dependence of the cessation threshold on the transport parameters by approximating v_s^+ by

its value at the Stokes drag limit, $v_s^+(d^+, s, c^+) \propto f_{Kn} d^{+2}$ (Materials and Methods), where the effects of rarefaction are contained within the Knudsen number-dependent Cunningham correction factor $f_{Kn}(Kn) \equiv 1 + Kn[2.49 + 0.84 \exp(-1.74/Kn)]$ (31). The normalized settling velocity $V_s^+ = s^{-1/3} v_s^+$ can then be approximated by the square of the normalized grain size $D^+(s, d^+, c^+) = f_{Kn}^{1/2} s^{-1/6} d^+$ (note that $f_{Kn}^{1/2} \simeq 1$ for $s \lesssim 10^5$). The scaling of the cessation threshold thus has the form $U_{*t}^+ = U_{*t}^+(D^+)$, which greatly simplifies the description of the cessation threshold for planetary saltation transport, overlapping numerical simulation data (Fig. 2(a)), experimental cessation threshold data (33–38) (Fig. 2(b), including cohesive aeolian conditions) and the predictions of the cessation threshold model (Fig. 2(a)-(c)). The cessation threshold model reproduces both numerical simulations and experimental data using slightly different parameters, referred to here as “simulation version” and “real-world version”, respectively (see Materials and Methods for details). For comparisons between model and oil and water threshold data, see Pähzt et al. (16). Note that the simple relationship

$$U_{*t}^+ = \frac{\min U_{*t}^+}{2} \left(\frac{D_{\min}^+}{D^+} + \frac{D^+}{D_{\min}^+} \right) \quad (1)$$

fits both numerical and experimental data of U_{*t}^+ near the cessation threshold minimum relatively well (Fig. 2(a)-(b)), where D_{\min}^+ and $\min U_{*t}^+$ denote the location and magnitude, respectively, of the cessation threshold minimum in the (D^+, U_{*t}^+) -plane, and may therefore be put to good use in future studies of planetary sediment transport.

The analysis above relies on scale-free boundary conditions, implying that the bed escape velocity v_b that a bed grain needs to exceed to enter the transport layer ($v_b \propto \sqrt{gd}$ in the absence of cohesion (11)) is not relevant for steady state saltation. Since v_b is strongly affected by cohesion (11), the scale-free boundary condition reflects the cohesion-insensitivity of the saltation dynamics. This is reinforced by the scaling of the average transport layer thickness at the threshold \bar{z}_t (Fig. S1(a)), which for saltation is nearly entirely due to the hopping motion of

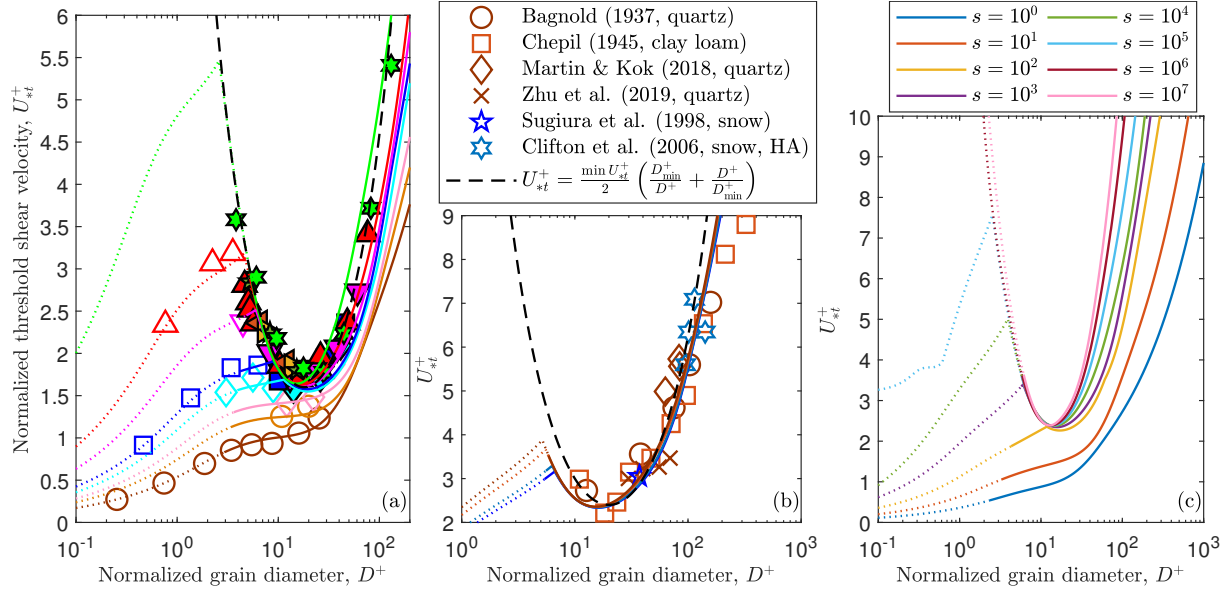


Figure 2: Scaling of saltation cessation threshold. Normalized threshold shear velocity $U_{*t}^+ = s^{-1/3} u_{*t}^+$, with $u_{*t}^+ = u_{*t} / \sqrt{\tilde{g} d_\mu}$, versus normalized grain size $D^+ = f_{Kn}^{1/2} s^{-1/6} d^+$, where $f_{Kn}^{1/2} \simeq 1$ in (a) and (b) because of $s < 10^5$. Symbols in (a) correspond to numerical simulations for various combinations of the density ratio $s \equiv \rho_p / \rho_f \in [2.65, 5 \times 10^4]$ and rescaled grain size $d^+ = d / d_\mu$, with open and filled symbols indicating bedload and saltation conditions, respectively (see Fig. S1 for simulation phase space). Symbols in (b) correspond to experimental cessation threshold data of terrestrial aeolian saltation of quartz (33–35), clay loam (36) and snow at high altitude (HA) (38) and sea level (37). Colored lines correspond to (a) the simulation version and (b) and (c) real-world version of the cessation threshold model. The solid colored lines indicate, for threshold conditions, a Rouse number $Ro_t \equiv v_s / u_{*t} \geq 0.5$ (bedload or saltation). The dotted colored lines indicate $Ro_t < 0.5$ (suspension). The kinks in the colored lines correspond to the bedload-saltation transition for nonsuspended conditions. The dashed black lines correspond to the fit $U_{*t}^+ = \frac{1}{2} \min U_{*t}^+ \left(\frac{D_{\min}^+}{D^+} + \frac{D^+}{D_{\min}^+} \right)$, with (a) $(D_{\min}^+, \min U_{*t}^+) = (18, 1.6)$ and (b) $(D_{\min}^+, \min U_{*t}^+) = (20, 2.4)$. Note that the minimum of U_{*t}^+ does not coincide with the well-known minimum of the threshold Shields number Θ_t , which occurs around $D^+ \approx 70$ for Earth’s atmospheric conditions. In particular, experimental data points with the smallest D^+ in (b) by Bagnold (33) and Chepil (36) exhibit a factor 2 to 3 larger Θ_t than the minimum of Θ_t (not shown), which was previously attributed to increasing cohesion with decreasing d . However, the cohesionless cessation threshold model captures these data because the larger values of Θ_t are actually a signature of viscous sublayer-driven saltation. Consistently, the data point by Sugiura et al., which corresponds to experiments with potentially very cohesive old snow (37), is also captured by the cessation threshold model.

transported grains ($\bar{z}_t \simeq \bar{v}_{z_t}^2 / \tilde{g}$), whereas for bedload, grains moving in enduring contacts with the bed surface (e.g., via rolling and sliding) cause a significant additional contribution to \bar{z}_t

due to the heterogeneity of the bed surface at the grain scale: $\bar{z}_t \simeq 0.3d + \overline{v_{zt}^2}/\tilde{g}$ (Fig. S1(a)). During enduring grain-bed contacts, transported grains have sufficient time to form cohesive bonds with the bed grains, which is the reason why the insensitivity of sediment transport to cohesion is limited to saltation but does not apply to bedload (16).

Consequently, the most mobile grain size $d^{\min} \simeq 13f_{Kn}^{-1/2}s^{1/6}d_\mu$ (i.e., normalized grain size $D^+(s, d^+, c^+) = 13$) corresponding to the saltation cessation threshold minimum $u_{*t}^{\min}(s) \simeq 2.54s^{1/3}\sqrt{\tilde{g}d_\mu}$ (Figs. 2(b)-(c)), predicted by the cessation threshold model, follows purely from hydrodynamics and not from the onset of cohesion at small grain sizes as previously thought (11). Interestingly, d^{\min} depends only weakly on the atmospheric conditions and changes only by a factor of 3.6 (in the range 80–290 μm) for Solar System bodies.

The relation between U_{*t}^+ and V_s^+ also has implications for the scaling of the transition between saltation and turbulent suspensions at the transport threshold, as defined by the critical Rouse number $Ro_t \equiv v_s/u_{*t} = 0.5$ (Materials and Methods). The ratio of the threshold shear and settling velocity is mainly a function of V_s^+ and thus on the normalized grain size D^+ . Therefore, the grain size at the saltation-suspension transition $d^{\text{sus}} \simeq 6f_{Kn}^{-1/2}s^{1/6}d_\mu$ (i.e., normalized grain size $D^+(s, d^+, c^+) = 6$) exhibits the same scaling as d^{\min} .

Sediment transport rate and phase diagrams. The results from the cessation threshold model are used to parametrize an existing analytical formulation for the equilibrium transport rate (19) and a new formulation for the impact kinetic energy flux (Materials and Methods). The transport rate equation parametrized by the threshold model reproduces the results of numerical simulations, for both aeolian and subaqueous conditions (Figure 3(a)), aeolian measurements (37, 39–42) (Fig. 3(b)) and subaqueous measurements (43–46) (Fig. 3(c)) for a wide range of conditions. We use the transport rate model coupled with the transport cessation threshold model to derive phase diagrams of planetary sediment transport and interpret the results.

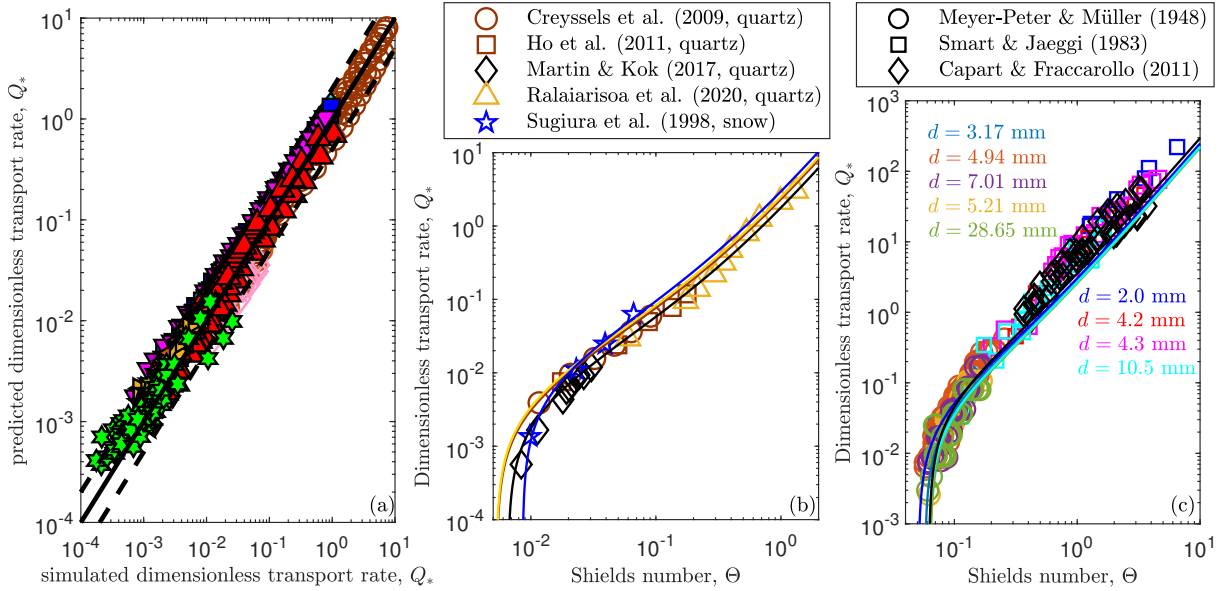


Figure 3: Validation of predicted transport rates. (a) Comparison of dimensionless sediment transport rates $Q_* = Q/(\rho_p d \sqrt{s \bar{g} d})$ from numerical simulations and from the simulation version of the analytical model (Materials and Methods). (b) and (c) Q_* versus Shields number $\Theta \equiv u_*^2/(s \bar{g} d)$. Symbols in (a) correspond to numerical simulations for various combinations of the density ratio $s \equiv \rho_p/\rho_f \in [2.65, 5 \times 10^4]$ and rescaled grain size $d^+ = d/d_\mu$, with $d^+ \gtrsim 6$ for $s \lesssim 10$ and $d^+ \gtrsim 17$ for $s \gtrsim 10$, and various Θ , where open and filled symbols indicate bedload and saltation conditions, respectively (see Fig. S1 for simulation phase space). Symbols in (b) and (c) correspond to experimental data of (b) aeolian (37, 39–42) and (c) fluvial (43, 44) sediment transport. Data by Meyer-Peter & Müller (43) are as corrected by Wong & Parker (46) and data by Smart & Jaeggi (44) and Capart & Fraccarollo (45) are corrected for sidewall drag and bed slopes as described by Pähzt et al. (16). The solid line in (a) indicates perfect agreement. The dashed lines in (a) indicate a deviation by a factor of 2. The lines in (b) and (c) correspond to the predictions of the real-world version of the analytical model.

Solar System bodies with known active aeolian processes are Venus, Titan, Earth and Mars (2, 4). Furthermore, active aeolian processes are also suspected on Triton (6) and Pluto (7). The atmospheric transport conditions on all these planetary bodies are highlighted in Fig. 4. Given the relative constancy of the rescaled speed of sound c^+ for Solar System bodies (Table S2), the rescaled shear velocity at the cessation threshold u_{*t}^+ is only function of the rescaled grain size d^+ and density ratio s (Fig. 4(a), transport modes are defined in the Materials and Methods). For the nonsuspended sediment transport rate, we reduced the three-dimensional phase

space (s , d^+ and u_*^+) by taking the average rate $\bar{Q}^d \equiv \int_{d_1^+}^{d_2^+} Q d d^+ / (d_2^+ - d_1^+)$, over the range of rescaled grain sizes $(d_1^+, d_2^+) = (10, 1000)$. We also replace the rescaled fluid shear velocity u_*^+ by the rescaled wind speed $U^+ = U(u_*^+, s, d^+) / \sqrt{\tilde{g} d}$ calculated using the law of the wall (Materials and Methods) at an elevation $5 \times 10^6 d_\mu \approx 10$ m above the bed surface ($d_\mu \approx 2 \mu\text{m}$ for most Solar System bodies). Interpreting U as the characteristic velocity of the strongest storms that occur over erodible surfaces on a given Solar System body (Table S1), the rescaled average transport rate $\bar{Q}^{d+}(U^+, s) = \bar{Q}^d / [\rho_p d_\mu (\tilde{g} d_\mu)^{1/2}]$ represents an estimation of the sediment transport potential (Fig. 4(b)). Below, we discuss a few important takeaways from these phase diagrams.

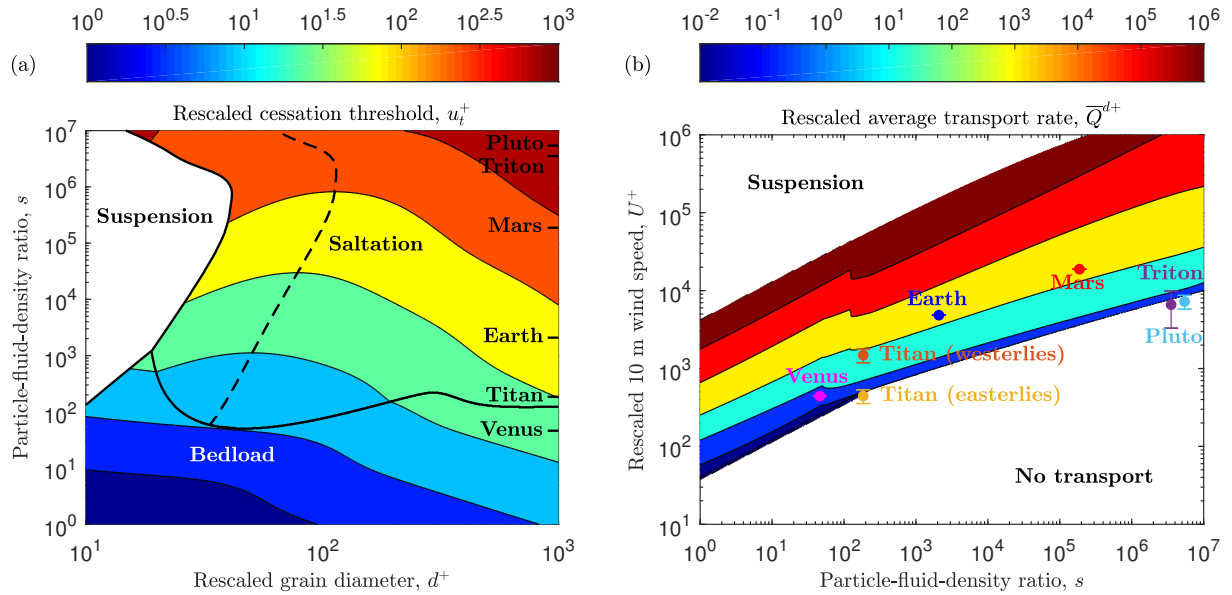


Figure 4: **Phase diagrams of planetary sediment transport predicted by model.** (a) Rescaled cessation threshold $u_*^+ = u_{*t} / \sqrt{\tilde{g} d_\mu}$ (color map) as function of the rescaled grain size $d^+ = d/d_\mu$ and particle-fluid-density ratio $s \equiv \rho_p/\rho_f$. (b) Rescaled average sediment transport rate $\bar{Q}^{d+} = \bar{Q}^d / [\rho_p d_\mu (\tilde{g} d_\mu)^{1/2}]$ (color map) as a function of the rescaled 10 m wind speed $U^+ = U / \sqrt{\tilde{g} d_\mu}$ and s . Symbols and error bars indicate the strongest storms that occur on a given Solar System body over erodible surfaces (excluding tropical storms on Earth over water). The solid lines in (a) indicate the suspension-saltation and bedload-saltation transitions (see Materials and Methods for definition). The dashed line in (a) corresponds to the minimum of u_*^+ for saltation conditions.

Discussion

Eastward dune propagation on Titan. Aeolian bedload, which is affected by cohesion, is predicted to occur mainly on Venus (Fig. 4(a)). In contrast, aeolian saltation, for which cohesion does not play a significant role (13) (as discussed earlier), is predicted to dominate all other conditions, including most conditions on Titan (Fig. 4(a)). These predictions contrast previous studies associating Titan with bedload transport (2) and with potentially very large effects of cohesion (14, 15). However, as can be seen in Fig. 4(b), despite its insensitivity to cohesion, the threshold minimum on Titan, which corresponds to the boundary between transport and no transport, is predicted to be between the strength of the strongest westward propagating storms (easterlies), associated with the general circulation on Titan, and rare eastward propagating methane storms (47) (westerlies). This behaviour is, indeed, required for consistency with the eastward propagation of Titan’s dunes. Previous attempts to explain this behaviour (47) were based on a cohesion-affected saltation threshold model that assumes that Titan’s and Earth’s surface materials are similarly cohesive (3). However, recent studies have suggested that Titan’s surface material may actually be much more cohesive than Earth’s surface material (14, 15), challenging these previous explanation attempts.

Solar System bodies with active dust cycle. Grain-bed impacts of saltating grains is one of the main drivers of dust emission (2). Our model predicts that, among the Solar System bodies that permit saltation (i.e., excluding bedload on Venus), only winds on Earth, Mars and Titan can exhibit substantial saltation transport potentials (Fig. 4(b)) and associated dust emission potentials (Fig. S3). Indeed, active dust cycles are well established for Earth and Mars (2) and have recently also been evidenced on Titan using spectral data from the Cassini spacecraft (48).

Saltation on Solar System bodies with very low air density. There has been some controversy about whether low-air-density Solar System bodies, such as Triton and Pluto, exhibit active aeolian processes, such as wind-blown dust (6) and even active dune formation and evolution (7). Our model predicts that this may, indeed, be the case to a marginal degree (Fig. 4(b)). In particular, the most mobile grain size on Pluto ($d^{\min} \simeq 85d_\mu \simeq 262 \mu\text{m}$, Fig. 4(a)) is consistent with grain size estimates obtained from measurements of the adsorption width of Pluto's supposed dune fields using New Horizons' Multi-Spectral Visible Imaging Camera (7). Note that this relatively small most mobile grain size is associated with rarefaction effects. Without such effects, the cessation threshold model would predict a substantially larger most mobile grain size ($d^{\min} \simeq 150d_\mu \simeq 462 \mu\text{m}$), inconsistent with the observations.

Materials and Methods

Physical quantities and dimensionless numbers controlling sediment transport: grain density ρ_p , fluid density ρ_f , median grain diameter d , fluid dynamic viscosity μ , fluid shear velocity u_* , speed of sound c and gravitational constant g , or its buoyancy-reduced value $\tilde{g} \equiv (1 - \rho_f/\rho_p)g$. Relevant dimensionless numbers: particle-fluid-density ratio $s \equiv \rho_p/\rho_f$, Galileo number $Ga = \rho_f \sqrt{s\tilde{g}d^3}/\mu$, Shields number $\Theta \equiv u_*^2/(s\tilde{g}d)$ and Knudsen number $Kn = \sqrt{k\pi/2}\mu/(\rho_f c d)$, with adiabatic exponent k . When expressed in terms of the alternative dimensionless numbers $d^+ = d/d_\mu$, $u_*^+ = u_*/\sqrt{\tilde{g}d_\mu}$ and $c^+ = c/\sqrt{\tilde{g}d_\mu}$ introduced in the main text (with $d_\mu \equiv [\mu/(\rho_p\sqrt{\tilde{g}})]^{2/3}$), the Galileo number becomes $Ga = s^{-1/2}d^{+3/2}$, the Shields number $\Theta = u_*^{+2}/(sd^+)$ and the Knudsen number $Kn = 1.48 s/(c^+d^+)$ for diatomic gases ($k = 1.4$).

Numerical simulations. Below we briefly describe the numerical model and define quantities used in model validation. Numerical simulations were performed for planetary conditions

within the range $s \in [2.65, 5 \times 10^4]$, $Ga \in [0.1, 100]$ and $\Theta \in (1, 100)\Theta_t$, where Θ_t is the cessation threshold Shields number (see below for its estimation).

Numerical model. We use the numerical model of Durán et al. (21) (modified as described in Pähzt & Durán (49)), which couples a discrete element method for the particle motion under gravity, buoyancy and fluid drag with a continuum Reynolds-averaged description of hydrodynamics. Spherical particles ($\sim 10^4$) with mild polydispersity are confined in a quasi-two-dimensional domain of length $\sim 10^3 d$ (where d is the mean particle diameter), with periodic boundary conditions in the flow direction, and interact via normal repulsion (restitution coefficient $e = 0.9$) and tangential friction (contact friction coefficient $\mu_c = 0.5$). The bottom-most particle layer is glued on a bottom wall, while the top of the simulation domain is reflective but so high that it is never reached by transported particles. The Reynolds-averaged Navier-Stokes equations are combined with a semiempirical mixing length closure that ensures a smooth hydrodynamic transition from high to low particle concentration at the bed surface and quantitatively reproduces the mean turbulent flow velocity profile in the absence of transport. Simulations with this numerical model are insensitive to e and therefore insensitive to viscous damping. The simulations reproduce measurements of the rate and threshold of aeolian transport, and viscous and turbulent subaqueous transport (Figs. 1 and 3 of Pähzt & Durán (18) and Fig. 4 of Pähzt & Durán (19)), height profiles of relevant equilibrium transport properties (Fig. 2 of Pähzt & Durán (18) and Fig. 6 of Durán et al. (50)) and aeolian ripple formation (51).

Average of simulated quantities. We define two types of averages for a particle property A_p . Based on the spatial homogeneity of the simulation, the mass-weighted average of A_p over all particles within a layer $(z, z + dz)$ and all time steps (after reaching steady state) is,

$$\langle A \rangle(z) = \sum_{z_p \in (z, z + dz)} m_p A_p / \sum_{z_p \in (z, z + dz)} m_p, \quad (2)$$

where m_p and z_p is the particle mass and elevation, respectively. We also define the average of a vertical profile $A(z)$ over the transport layer (called “transport-layer average” in figures and main text) as (18)

$$\bar{A} = \frac{\int_0^\infty \rho A(z) dz}{\int_0^\infty \rho dz}, \quad (3)$$

where $\rho(z)$ is the particle concentration and the bed surface elevation $z = 0$ is defined as the elevation at which $p_g d\langle v_x \rangle / dz$ is maximal (20), where $p_g(z) = -\int_z^\infty \rho \langle a_z \rangle dz'$ is the normal-bed granular pressure and \mathbf{a} the acceleration of grains by noncontact forces. This definition is used to calculate the transport layer thickness \bar{z} (with $A(z) = z$) and the characteristic hop height of transported grains \bar{v}_z^2 / \tilde{g} (with $A(z) = \langle v_z^2 \rangle / \tilde{g}$) among other quantities. Furthermore, we calculate the transport load (mass of transported particles per unit area) as $M = \int_0^\infty \rho dz$ and the transport rate as $Q = \int_{-\infty}^\infty \rho \langle v_x \rangle dz$, such that the average grain velocity in the flow direction is $\bar{v}_x \simeq Q/M$ because of $Q \simeq \int_0^\infty \rho \langle v_x \rangle dz$ (20).

Calculation of cessation threshold from simulation data. Based on the approximation of the transport rate as $Q \simeq M \bar{v}_x$, we extrapolate the Shields number value Θ_t at which Q vanishes using the linear relation between transport load M and Shields number Θ , $M \propto \Theta - \Theta_t$, where we treat Θ_t as a fit parameter (19–21). The rescaled threshold shear velocity $u_{*t}^+ = u_{*t} / \sqrt{\tilde{g} d_\mu}$ shown in Figs. 1 and 2 is calculated from Θ_t as $u_{*t}^+ = \sqrt{\Theta_t s d^+}$, with $d^+ = s^{1/3} G a^{2/3}$.

Cessation threshold model. The cessation threshold model of Pähzt et al. (16) combines an analytical (approximated) solution of the equations of motion of a grain moving under gravity and fluid drag, relating the impact velocity $\mathbf{v}_\downarrow = f_1(\mathbf{v}_\uparrow)$ to the lift-off (or rebound) velocity \mathbf{v}_\uparrow , with boundary conditions that describe the average outcome of a grain-bed rebound ($\mathbf{v}_\uparrow = f_2(\mathbf{v}_\downarrow)$). For given values of d^+ , s , c^+ and $v_{\uparrow z}$, the model then calculates the value of u_*^+ for which there is a periodic grain trajectory (i.e., $f_2^{-1} = f_1$) with a rebound kinetic energy high

enough to escape from the bed when assisted by the near surface flow. The cessation threshold u_{*t}^+ is then defined as the minimum u_*^+ for which such a solution exist.

The cessation threshold model exists in two different versions (16): a “real-world version” developed for three-dimensional conditions and calibrated using experimental data, and a “simulation version” that differs in the parameter values that describe the bed surface as the numerical simulations are quasi-two-dimensional (note that the predictions of both versions are qualitatively identical and quantitatively similar). Below, we derive the simplified equations of motion of an individual grain hopping within the inner turbulent boundary layer, describe the central elements of the model, and generalize it to include rarefaction effects.

Undisturbed flow velocity profile. Neglecting grain’s feedback on the flow close to the cessation threshold (16, 18), the mean flow velocity profile $u_x(z)$ within the inner turbulent boundary layer (the “law of the wall”) has the form,

$$u_x(z) = u_* f_u(z/\delta_\mu, d/\delta_\mu), \quad (4)$$

where $\delta_\mu = 10\mu/(\rho_f u_*) = 10sd_\mu/u_*^+$ is the thickness of the viscous sublayer (52), and the function f_u can be approximated as (16, 53)

$$f_u = 7 \arctan\left(\frac{R_z}{0.7}\right) + \frac{7}{3} \arctan^3\left(\frac{R_z}{0.7}\right) - 0.52 \arctan^4\left(\frac{R_z}{0.7}\right) + \ln\left[1 + \left(\frac{R_z}{9.482}\right)^{(1/\kappa)}\right] - \frac{1}{\kappa} \ln\left\{1 + 3d/\delta_\mu \left[1 - \exp\left(-\frac{5d/\delta_\mu}{13}\right)\right]\right\}, \quad (5)$$

where $R_z = (z + rd)/\delta_\mu$, $\kappa = 0.4$ is the von Kármán constant and $rd = 0.7d$ the distance between the bed surface elevation ($z = 0$) and the virtual zero-velocity elevation (i.e., $u_x(-rd) \simeq 0$). For saltation, when most grains are performing large hops and therefore $z \gg rd$ most of the time, Eq. (5) recovers the linear scaling $u_x \simeq 10u_*z/\delta_\mu$ within the viscous sublayer ($z/\delta_\mu \lesssim 1$), and the logarithmic scaling $u_x \simeq \kappa^{-1}u_* \ln(z/z_0)$ within the log-layer ($z/\delta_\mu \gtrsim 1$),

where the roughness $z_0 \simeq \delta_\mu/90$ for hydrodynamically smooth conditions ($d/\delta_\mu \lesssim 0.4$) and $z_0 \simeq d/30$ for hydrodynamically rough conditions ($d/\delta_\mu \gtrsim 7$). Furthermore, for smooth saltation, the last term in Eq. (5) is negligible and we can approximate $f_u(z/\delta_\mu, d/\delta_\mu) \simeq f_u(z/\delta_\mu, 0)$.

Drag acceleration. Defining the relative flow velocity as $\mathbf{u}_r = \mathbf{u} - \mathbf{v}$, where \mathbf{u} and \mathbf{v} are the fluid and grain velocities, respectively, the fluid drag acceleration \mathbf{a}^d has the form,

$$\mathbf{a}^d = \frac{3}{4sd} C_d |\mathbf{u}_r| \mathbf{u}_r, \quad (6)$$

where the drag coefficient C_d is a function of the Reynolds number $\text{Re}_r \equiv \rho_f |\mathbf{u}_r| d / \mu$. To account for rarefaction effects, we use the drag parametrization of Crowe et al. (31) in terms of the Mach number $\text{Ma}_r = |\mathbf{u}_r|/c$, where c is the speed of sound. Using the Knudsen number $Kn = \sqrt{k\pi/2} \mu / (\rho_f c d)$ (k is the adiabatic exponent), we can express the Mach number in terms of the Reynolds number as $\text{Ma}_r = \text{Re}_r Kn / \sqrt{k\pi/2}$. The drag coefficient C_d including rarefaction effects can then be approximated as,

$$C_d(\text{Re}_r, Kn) = 2 + (C_{d0}(\text{Re}_r) - 2) e^{-2.45 h_1 Kn} + \frac{h_2}{\text{Re}_r Kn} \exp\left(-\frac{0.74}{Kn}\right), \quad (7)$$

where h_1 and h_2 are the functions,

$$h_1 = \frac{1 + \text{Re}_r(12.278 + 0.548\text{Re}_r)}{1 + 11.278\text{Re}_r},$$

$$h_2 = \frac{7.0}{1 + 0.67\text{Re}_r Kn} + 2.1,$$

and we have used $k = 1.4$ for diatomic gases. C_{d0} is the drag coefficient in the no-rarefaction limit ($Kn = 0$) and can be approximated for spherical grains as (54)

$$C_{d0}(\text{Re}_r) = \left(\sqrt{24/\text{Re}_r} + \sqrt{C_d^\infty} \right)^2, \quad (8)$$

where $C_d^\infty = 0.4$ corresponds to the limit at large Re_r .

In order to simplify the problem for analytical treatment, we linearize the drag acceleration \mathbf{a}^d approximating $|\mathbf{u}_r| = |\mathbf{u} - \mathbf{v}|$ by the average along the flow direction $\overline{u_{r,x}} = \overline{u_x} - \overline{v_x}$, where the overline represents the average over a grain trajectory of hop time T , e.g., $\overline{v_x} = \frac{1}{T} \int_0^T v_x(t) dt$ (for justifications of this simplification, see Pähzt et al. (16)). This yields,

$$\mathbf{a}^d \approx \frac{3}{4sd} C_d(\overline{\text{Re}_r}, Kn) \overline{u_{r,x}} \mathbf{u}_r, \quad (9)$$

where $\overline{\text{Re}_r} \equiv \rho_f \overline{u_{r,x}} d / \mu$. From the definition of the settling velocity v_s ($v_s = -v_z$ when $a_z^d = \tilde{g}$), the identity $\mathbf{a}^d = \overline{a_x^d} \mathbf{u}_r / \overline{u_{r,x}}$ and the condition $u_z = 0$, we obtain

$$v_s = \overline{u_{r,x}} / \left(\overline{a_x^d} / \tilde{g} \right) \quad (10)$$

and the linearized drag acceleration can be written in terms of the settling velocity as

$$\frac{\mathbf{a}^d}{\tilde{g}} = \frac{\mathbf{u}_r}{v_s} = \frac{\mathbf{u} - \mathbf{v}}{v_s}. \quad (11)$$

Settling velocity in the cessation threshold model. The settling velocity is obtained from Eq. (10) after defining an effective bed friction coefficient $\mu_b = \overline{a_x^d} / \tilde{g}$ and calculating the average relative streamwise flow velocity $\overline{u_{r,x}}$ from the implicit equation

$$\frac{\overline{a_x^d}}{\mu_b \tilde{g}} = \frac{3C_d(\overline{\text{Re}_r}, Kn) \overline{u_{r,x}}^2}{4\mu_b s \tilde{g} d} = 1, \quad (12)$$

arising from the definition of μ_b . Introducing the rescaled velocity $u_r^+ = \overline{u_{r,x}} / \sqrt{\tilde{g} d_\mu}$, we get an implicit equation for u_r^+ in terms of the relevant dimensionless numbers d^+ , s and c^+ ,

$$C_d(\overline{\text{Re}_r}, Kn) u_r^{+2} = \frac{4\mu_b}{3} s d^+, \quad (13)$$

where $\overline{\text{Re}_r}(u_r^+) = u_r^+ d^+ / s$, $Kn = 1.48s/(c^+ d^+)$ and C_d is given by Eqs. (7) and (8). The rescaled settling velocity $v_s^+ = v_s / \sqrt{\tilde{g} d_\mu}$ thus has the form (we keep the Knudsen number as Kn for simplicity),

$$v_s^+ = \mu_b^{-1} u_r^+(d^+, s, Kn). \quad (14)$$

Extensive numerical simulations and analytical calculations have shown that the friction coefficient μ_b can be well approximated by a constant (16, 20, 21), which means that the settling velocity as defined here is independent on the grain trajectory.

Settling velocity for the analysis of simulation data. Since the numerical simulations neglect rarefaction effects ($Kn = 0$), $C_d = C_{d0}$ and Eq. (13) can be solved analytically, which leads, after substituting into Eq. (14) and rearranging terms, to

$$v_s^+(d^+, s) = A \left[\left(1 + 2\sqrt{\frac{d^{+2}}{18A}} \right)^{1/2} - 1 \right]^2, \quad (15)$$

with $A(d^+, s) = 6s/(C_d^\infty \mu_b d^+)$. This formulation is used to calculate v_s^+ from simulation data (using $\mu_b = 0.63$ (16, 20)) as shown in Fig. 1(b).

Settling velocity in the Stokes drag limit including rarefaction. For relatively small Galileo numbers Ga , as is the case for transport close to the cessation threshold near the minimum in Fig. 1(b), v_s^+ can be approximated by its value in the Stokes drag limit. Substituting $C_{d0} \approx 24/\text{Re}_r$ in Eq. (7) and using Eqs. (13) and (14), we get

$$v_s^+ = f_{Kn} d^{+2}/18, \quad (16)$$

where $f_{Kn}(Kn) \equiv 1 + Kn[2.49 + 0.84 \exp(-1.74/Kn)]$ is the Cunningham correction factor (31).

Equations of motion. The equations of motion of a transported grain under gravity (vertical acceleration $-\tilde{g}$) and fluid drag (acceleration \mathbf{a}^d given by Eq. (11)) are

$$\begin{aligned} \frac{d\hat{v}_x}{d\hat{t}} &= \hat{u}_x(\hat{z}) - \hat{v}_x, \\ \frac{d\hat{v}_z}{d\hat{t}} &= -1 - \hat{v}_z, \end{aligned} \quad (17)$$

where the hat indicates quantities rescaled using \tilde{g} and v_s . The rescaled fluid velocity \hat{u}_x is

$$\hat{u}_x(\hat{z}) = \hat{u}_* f_u \left(\hat{z}/\hat{\delta}_\mu, d/\delta_\mu \right), \quad (18)$$

with rescaled viscous sublayer thickness $\hat{\delta}_\mu = \delta_\mu \tilde{g} / v_s^2$ and the function f_u given by Eq. (5). For a given initial condition, the grain's trajectory is thus defined by three dimensionless numbers relating u_*^+ , d^+ , s and the rescaled settling velocity v_s^+ : $\hat{u}_* \equiv u_*^+ / v_s^+$, $d/\delta_\mu \equiv u_*^+ d^+ / (10 s)$ and $\hat{\delta}_\mu \equiv 10 s / (u_*^+ v_s^{+2})$.

An important conceptual simplification is achieved by introducing the normalized velocities, $U_*^+ = s^{-1/3} u_*^+$ and $V_s^+ = s^{-1/3} v_s^+$, and neglecting in a first approximation the dependence of the fluid velocity \hat{u}_x on d/δ_μ for transitional or hydrodynamically smooth flows. This eliminates the explicit dependence of \hat{u}_x on the particle-fluid-density ratio s :

$$\hat{u}_x \approx \hat{u}_x(\hat{z} | U_*^+, V_s^+) = (U_*^+ / V_s^+) f_u \left(\hat{z}/\hat{\delta}_\mu, 0 \right), \quad (19)$$

with $\hat{\delta}_\mu = 10 / (U_*^+ V_s^{+2})$. Therefore, the rescaled impact grain velocity $\hat{\mathbf{v}}_\downarrow$ depends only on the rescaled lift-off velocity $\hat{\mathbf{v}}_\uparrow$, U_*^+ and V_s^+ ,

$$\hat{\mathbf{v}}_\downarrow = f_1(\hat{\mathbf{v}}_\uparrow | U_*^+, V_s^+). \quad (20)$$

Relation between U_{*t}^+ and V_s^+ . Combining Eq. (20) with two further relations, a scale-free rebound boundary condition of the type $\hat{\mathbf{v}}_\uparrow = f_2(\hat{\mathbf{v}}_\downarrow)$ and the cessation threshold condition, which imposes an additional constraint on grain's trajectory of the type $\hat{\mathbf{v}}_\uparrow = f_3(U_*^+, V_s^+)$ (see below for a precise definition), we get that, at the cessation threshold, the normalized shear velocity $U_*^+ = U_{*t}^+$ depends only on the normalized settling velocity V_s^+ .

Relation between U_{*t}^+ and $\bar{z}_t/\delta_{\mu t}$. Numerical simulations show that the average vertical grain velocity at the threshold, defined as $\sqrt{\bar{v}_{zt}^2}$, is proportional to the transport-layer averaged flow velocity $\bar{u}_{xt} = u_{*t} f_u(\bar{z}_t/\delta_{\mu t}, d/\delta_{\mu t})$ (Fig. S2), where \bar{z}_t is the transport layer thickness at the

threshold and $\delta_{\mu t} = 10sd_{\mu}/u_{*t}^+$ the viscous sublayer thickness at the threshold. Furthermore, for saltation close to the threshold, \bar{z}_t scales with the average hop height of grain trajectories, $\bar{z}_t \approx \bar{v}_{zt}^2/\tilde{g}$ (Fig. S1(a)). Combining these relations, we get

$$\frac{1}{U_t^{+3}} \left(\frac{\bar{z}_t}{\delta_{\mu t}} \right) \approx \frac{\bar{v}_{zt}^2}{u_{*t}^2} \propto \left(\frac{\bar{u}_{xt}}{u_{*t}^2} \right)^2 = f_u^2 \left(\frac{\bar{z}_t}{\delta_{\mu t}}, \frac{d}{\delta_{\mu t}} \right), \quad (21)$$

which leads to a relation between U_{*t}^+ and the rescaled transport layer thickness $\bar{z}_{t\delta} = \bar{z}_t/\delta_{\mu t}$ of the form

$$U_{*t}^+ \propto \left(\frac{\bar{z}_{t\delta}}{f_u^2(\bar{z}_{t\delta}, d/\delta_{\mu t})} \right)^{1/3}. \quad (22)$$

Assuming the flow is hydrodynamically smooth ($d/\delta_{\mu t} \ll 1$), when sediment transport extends above the viscous sublayer into the so-called log-layer ($\bar{z}_{t\delta} > 1$), the average flow velocity is logarithmic ($f_u(\bar{z}_{t\delta}, 0) \propto \ln \bar{z}_{t\delta}$), and the normalized threshold shear velocity U_{*t}^+ increases approximately as $\bar{z}_{t\delta}^{-1/3}$. In contrast, when transport takes place mainly within the viscous sublayer ($\bar{z}_{t\delta} < 1$), the flow velocity increases linearly with elevation ($f_u(\bar{z}_{t\delta}, 0) \approx \bar{z}_{t\delta}$) and the normalized threshold shear velocity U_{*t}^+ decreases as $\bar{z}_{t\delta}^{-1/3}$ (Fig. 1(c)).

Analytical solution for periodic trajectories. For a given lift-off, or rebound, rescaled vertical velocity $\hat{v}_{\uparrow z}$, the rescaled vertical impact velocity $\hat{v}_{\downarrow z}$ is calculated from integrating the vertical grain acceleration (16):

$$\hat{v}_{\downarrow z} = -1 - W \left[-(1 + \hat{v}_{\uparrow z}) e^{-(1 + \hat{v}_{\uparrow z})} \right], \quad (23)$$

where W denotes the principal branch of the Lambert- W function. Assuming periodic trajectories, the rescaled impact and rebound streamwise velocities, $\hat{v}_{\downarrow x}$ and $\hat{v}_{\uparrow x}$, are then calculated from the boundary conditions (16):

$$\begin{aligned} \frac{|\hat{\mathbf{v}}_{\uparrow}|}{|\hat{\mathbf{v}}_{\downarrow}|} &= A_r + B_r \frac{\hat{v}_{\downarrow z}}{|\hat{\mathbf{v}}_{\downarrow}|}, \\ -\frac{\hat{v}_{\uparrow z}}{\hat{v}_{\downarrow z}} &= (A_r + C_r) / \sqrt{-\frac{\hat{v}_{\downarrow z}}{|\hat{\mathbf{v}}_{\downarrow}|} - (B_r + C_r)}, \end{aligned} \quad (24)$$

where two sets of parameters A_r , B_r and C_r are used depending on whether the model is compared to real data or the numerical model (16) (see below for the precise values). Impact and rebound velocities are then used to calculate the friction coefficient μ_b for a given trajectory as,

$$\mu_b \equiv \frac{\overline{a_x^d}}{\tilde{g}} = -\frac{\overline{a_x}}{\overline{a_z}} = \frac{\hat{v}_{\downarrow x} - \hat{v}_{\uparrow x}}{\hat{v}_{\downarrow z} - \hat{v}_{\uparrow z}}, \quad (25)$$

where we used $\overline{a_z^d} \propto -\overline{v_z} = 0$. Using the calculated μ_b , the rescaled settling velocity v_s^+ is obtained from Eqs. (13) and (14) as a function of d^+ , s and c^+ .

The rescaled fluid shear velocity u_*^+ corresponding to the periodic trajectory parametrized by $\hat{v}_{\uparrow z}$ is given by an implicit equation that follows from the integration of the streamwise grain acceleration (16):

$$\hat{u}_x(\hat{z}_{\text{eff}}|u_*^+, v_s^+, d^+, s) = \mu_b(1 + \hat{v}_{\uparrow z}) + \hat{v}_{\uparrow x}, \quad (26)$$

where $\hat{u}_x(\hat{z}_{\text{eff}})$ is given by Eq. (18) and \hat{z}_{eff} is an effective height defined as $\hat{z}_{\text{eff}} \equiv -\hat{v}_{\downarrow z}(1 + \hat{v}_{\uparrow z}) - \hat{v}_{\uparrow z}$. Finally, the average streamwise grain velocity $\hat{\bar{v}}_x$ is calculated from Eq. (14) as:

$$\hat{\bar{v}}_x = \hat{u}_x(\hat{z}|u_*^+, v_s^+, d^+, s) - \mu_b, \quad (27)$$

where $\hat{\bar{z}} = (\hat{v}_{\uparrow z} + \hat{v}_{\downarrow z})/2$ is the average height of the trajectory.

Cessation Threshold. The rescaled cessation threshold $u_{*t}^+ = u_{*t}^+(d^+, s, c^+)$ is defined as the minimum u_*^+ for which there is a periodic trajectory with a rebound kinetic energy $E_{\uparrow} = \frac{1}{2}mv_{\uparrow}^2$, with grain mass m , larger than the potential energy $E_b(\Theta)$ necessary to escape the most stable pockets of the bed surface when assisted by the near surface flow (16):

$$E_b(\Theta) = \left(\frac{1}{\sqrt{1 + \cot^2 \psi_Y(\Theta^2/\Theta_Y^2)}} - \sin \psi_Y \right) m\tilde{g}d, \quad (28)$$

where $\psi_Y = 25^\circ$ and we use different values for Θ_Y to fit either real data or numerical simulations (16) (see below). Quantities corresponding to this threshold solution are indicated by a subscript “t”.

“Real-world version” of the cessation threshold model. The following parameters are used to reproduce measurements and generate predictions for planetary transport (Figs. 2(b)-(c), 3(b)-(c), 4 and S3): $C_d^\infty = 0.4$ in Eq. (8); $A_r = 0.87$, $B_r = 0.72$ and $C_r = 0$ in Eq. (24); and $\Theta_Y = 0.13$ in Eq. (28).

“Simulation version” of the cessation threshold model. The following parameters are used when comparing to numerical simulations (Figs. 2(a), 3(a) and S1): $Kn = 0$ ($c^+ \rightarrow \infty$) in Eq. (7); $C_d^\infty = 0.5$ in Eq. (8); $A_r = 0.8$, $B_r = 0.3$ and $C_r = 0.3$ in Eq. (24); and $\Theta_Y = 0.18$ in Eq. (28).

Sediment transport rate formulation. The sediment transport rate Q as function of the Shields number Θ , valid if $d^+ \gtrsim 6$ for $s \lesssim 10$ and $d^+ \gtrsim 17$ for $s \gtrsim 10$, is given by (16, 19)

$$Q(\Theta) = \rho_p d \bar{v}_x|_t M_*(\Theta) [1 + 1.7M_*(\Theta)], \quad (29)$$

where $M_* = (\Theta - \Theta_t)/\mu_b = M/(\rho_p d)$ is the dimensionless mass of transported grains per unit bed area. The friction coefficient μ_b , the threshold Shields number $\Theta_t = u_t^{+2}/(sd^+)$ and the average streamwise grain velocity $\bar{v}_x|_t = \hat{v}_x|_t v_s$ are obtained from the cessation threshold model. For the calculation of the impact kinetic energy flux (below), we note that Eq. (29), after dividing by $M\bar{v}_x|_t = \rho_p d M_* \bar{v}_x|_t$ and using $\bar{v}_x \simeq Q/M$, can be rearranged to an approximate relation for the average streamwise grain velocity relative to its threshold value:

$$\bar{v}_x/\bar{v}_x|_t \simeq 1 + 1.7M_*. \quad (30)$$

Impact kinetic energy flux. The impact kinetic energy flux $Q_{E\downarrow}$ is defined as the kinetic energy of transported grains impacting the bed surface per unit bed area per unit time. In the context of (quasi)periodic saltation, the kinetic energy of saltating grains per unit bed area

$\frac{1}{2}M\mathbf{v}_\downarrow^2$ impacts the bed per duration of a saltation trajectory $T = (v_{z\uparrow} - v_{z\downarrow})/\tilde{g}$, and $Q_{E\downarrow}$ is therefore given by

$$Q_{E\downarrow} = \frac{M\tilde{g}(v_{\downarrow x}^2 + v_{\downarrow z}^2)}{2(v_{z\uparrow} - v_{z\downarrow})}. \quad (31)$$

From the cessation threshold model, we obtain M and the impact velocity components at the threshold, $v_{\downarrow x}|_t$ and $v_{\downarrow z}|_t$, while the ratios $v_{\downarrow x}/v_{\downarrow x}|_t$ and $v_{\downarrow z}/v_{\downarrow z}|_t$ are estimated analogous to Eq. (30):

$$\begin{aligned} v_{\downarrow x}/v_{\downarrow x}|_t &= 1 + 1.7M_*, \\ v_{\downarrow z}/v_{\downarrow z}|_t &= \sqrt{1 + 1.7M_*}. \end{aligned} \quad (32)$$

In Eq. (32), we made use of three insights: First, the equations of motion (Eq. (17)) in the streamwise and vertical directions are decoupled from each other as a consequence of the approximation Eq. (9). Second, transport layer-averaged velocities of (quasi)periodically saltating grains, such as \bar{v}_x and \bar{v}_z^2 , are strongly correlated with the rebound and impact velocities (16). In particular, if vertical drag can be neglected, $\bar{v}_x = \frac{1}{2}(v_{\uparrow x} + v_{\downarrow x}) \propto v_{\downarrow x}$ and $\bar{v}_z^2 = \frac{1}{3}v_{\uparrow z}^2 = \frac{1}{3}v_{\downarrow z}^2$. And third, numerical sediment transport simulations have shown that grain velocities in the vertical direction increase with the Shields number Θ like the square root of grain velocities in the streamwise direction (e.g., $\bar{v}_z^2 \propto \bar{v}_x|_t \bar{v}_x$ (18)). Using Eq. (32), Eq. (31) becomes

$$Q_{E\downarrow} = \frac{\rho_p d \tilde{g} M_*}{2(v_{z\uparrow}|_t - v_{z\downarrow}|_t)} [v_{\downarrow x}|_t (1 + 1.7M_*)^{3/2} + v_{\downarrow z}|_t (1 + 1.7M_*)^{1/2}]. \quad (33)$$

Transport modes. For the numerical simulations, we classify transport as bedload or saltation depending on whether the average hop height of transported grains \bar{v}_z^2/\tilde{g} exceeds or not the average grain size, with bedload for $\bar{v}_z^2/\tilde{g} < d$ and saltation for $\bar{v}_z^2/\tilde{g} \geq d$ (Fig. S1). In the cessation threshold model, we classify bedload or saltation transport based on whether fluid drag is essential for the periodic trajectory to escape the bed surface (16, 18). Bedload takes place when the rebound kinetic energy at the threshold $E_{\uparrow t}$ is below the bed potential energy in the absence of flow $E_b(0)$, i.e., $E_{\uparrow t} < E_b(0)$ (see Eq. (28) for definition of $E_b(\Theta)$), whereas

saltation takes place when $E_{\uparrow t} \geq E_b(0)$, in which case the grain’s kinetic energy is enough to escape the bed even in the absence of fluid drag. As shown in Fig. S1, both classifications, from the numerical simulations and the simulation version of the cessation threshold model, are in agreement. Although simulated transport is always nonsuspended (bedload or saltation), since both the numerical and analytical models neglect turbulent fluctuations around the mean turbulent flow, we can identify the onset of suspension in the cessation threshold model from the condition $Ro < 0.5$ based on the Rouse number $Ro \equiv v_s/u_*$. For aeolian saltation on Earth, this condition corresponds to $d \lesssim 40 \mu\text{m}$ at the threshold, which is within the short-term suspension regime classified by Kok et al. (2). Although the critical value 0.5 is smaller than those given in previous studies (e.g., $Ro < 1$ (52)), it is consistent with measurements showing largely nonsuspended aeolian sand transport for intense wind speeds close to $Ro = 0.5$ (42).

Supplementary Materials

Sediment transport initiation. In fluvial environments, sediment transport initiation is not an issue as rolling of grains can be initiated even an order of magnitude below the cessation threshold Shields number Θ_t (17). (Note that, even though Θ_t is called “cessation threshold”, sediment transport never completely vanishes below Θ_t (17).) In contrast, in aeolian environments, idealized wind tunnel experiments suggest that aeolian saltation is initiated at Shields numbers larger than Θ_t (17). Most researchers have therefore estimated the potential for aeolian saltation on extraterrestrial planetary bodies from initiation threshold measurements in wind tunnels with analogous atmospheric pressure conditions (3, 6, 14, 26, 27, 55, 56). However, since even a single airborne grain (readily generated in natural environments, see below) can trigger a collision chain resulting in self-sustained saltation provided that the fetch is long enough (typical for natural field conditions) (57), it has been argued that saltation initiation in the field may not be an issue once the cessation threshold is exceeded (7, 17, 30). This view-

point is supported by field observations of widespread and persistent transport of cohesive snow grains on Earth (58) and mineral grains on Mars (59, 60), which would be difficult to explain if saltation initiation was a real issue.

In natural environments, grains can become airborne much more easily than in idealized wind tunnel experiments for various reasons: First, topography inhomogeneities can cause bed grains to be highly exposed to the wind. Second, obstacles can dramatically enhance local turbulence, which is responsible for flow-driven entrainment (17). Third, even for idealized sediment beds, rare strong wind gusts associated with thick atmospheric boundary layers strongly increase the entrainment probability when compared with analogous conditions in wind tunnels (30). Fourth, wind may not even be needed because the sublimation of subsurface ice in cold environments (the so-called *solid-state greenhouse effect* (61)) can readily generate airborne grains of carbon dioxide, methane and nitrogen ice (6–8). For all these reasons, like a previous study (7), we do not consider the potential influence of saltation initiation on our estimations of extraterrestrial aeolian saltation.

Planetary body	Main gas(es)	Molar weight m_{mol} [g/mol]	Press. P [Pa]	Temp. T [K]	Sound speed c [m/s]	Storm speed U [m/s]
Venus (62)	CO ₂	43.5	9.2e6	737	428	2
Titan (47)	N ₂	28.6	1.5e5	94	195	0.9 (3)
Earth (63)	N ₂ /O ₂	28.97	1.0e5	293	343	20
Mars (64)	CO ₂	43.5	636	210	228	45
Triton (6, 65)	N ₂	28.0	1.65	38	126	10
Pluto (66)	N ₂	28.0	1.0	37	124	10

Table S1: **Overview over atmospheric conditions on Solar System bodies with observed or suspected aeolian processes.** Eastward directed storms (westerlies) on Titan are stronger than easterlies (47). The relative errors of U are estimated as 20% when U has been obtained from general circulation models (47) (Titan and Pluto) and 50% when obtained from theoretical reasoning (6, 65) (Triton). For direct observations of U (Venus, Earth and Mars), errors are small and therefore not estimated.

Planetary body	Particle density ρ_p [kg/m ³]	Fluid density ρ_f [kg/m ³]	Gravity g [m/s ²]	Viscosity μ [Pa · s]	d_μ [μm]	c^+
Venus	3000	65	8.87	3.2e-5	2.34	9.4e4
Titan	1000	5.4	1.35	6.2e-6	3.05	9.6e4
Earth	2500	1.2	9.81	1.8e-5	1.74	8.3e4
Mars	3000	1.6e-2	3.72	1.1e-5	1.53	9.5e4
Triton	494	1.4e-4	0.78	2.2e-6	2.94	8.3e4
Pluto	494	9.1e-5	0.62	2.1e-6	3.08	9.0e4
Earth (snow)	910	1.1	9.81	1.7e-5	3.29	6.0e4
Earth (snow, HA)	910	1.4	9.81	1.7e-5	3.29	6.0e4

Table S2: **Overview over environmental conditions on Solar System bodies with observed or suspected aeolian processes.** Values for Venus, Titan, Earth and Mars are very close to those given in Kok et al. (2). Values for Pluto are very close to those of Telfer et al. (7). Values for Triton are close to those of Sagan & Chyba (6), except for the particle density. We assumed that Triton's surface is composed of Methane ice ($\rho_p = 494$ kg/m³) because the value $\rho_p = 750$ kg/m³ of Sagan & Chyba (6) would yield predictions for Triton that are almost identical to those for Pluto. Conditions for snow transport on Earth are shown for completeness but are not displayed in the phase diagrams.

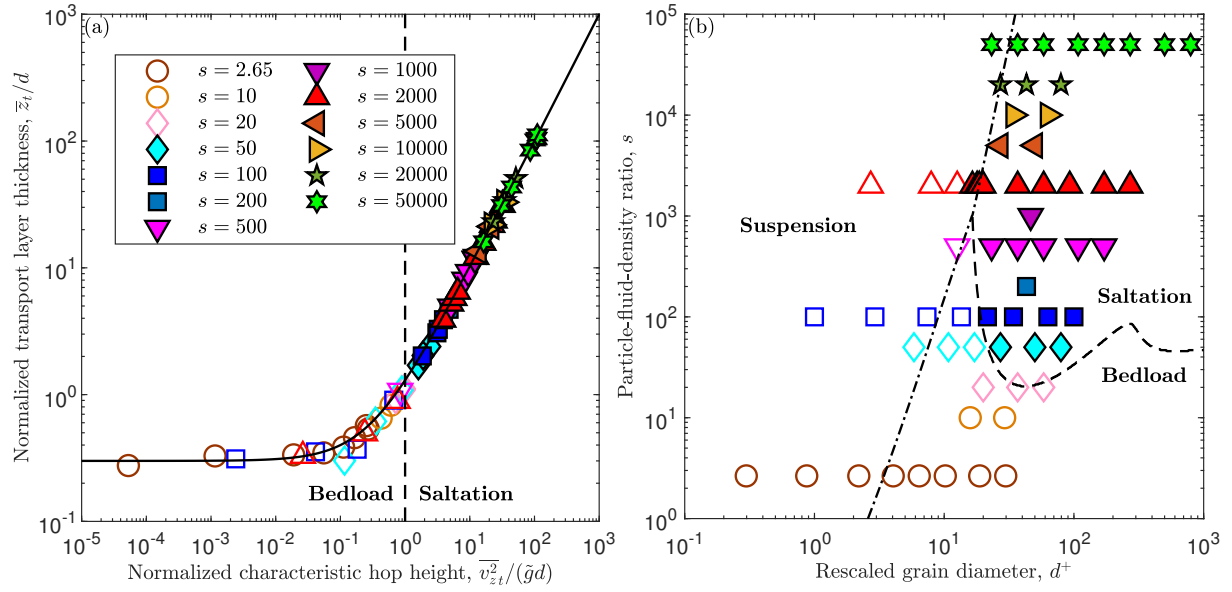


Figure S1: Sediment transport regimes for near-threshold conditions. (a) Transport layer thickness \bar{z}_t versus characteristic hop height of transported grains \bar{v}_z^2/\tilde{g} , both relative to the grain size d . (b) Summary of simulated conditions in terms of the density ratio $s \equiv \rho_p/\rho_f$ and rescaled grain size $d^+ = d/d_\mu$. Open and closed symbols correspond to simulation data for bedload and saltation conditions, respectively, as predicted by the simulation version of the cessation threshold model. The solid line in (a) corresponds to $\bar{z}_t = 0.3d + \bar{v}_{z_t}^2/\tilde{g}$. The dashed line in (a) indicates $\bar{v}_{z_t}^2/\tilde{g} = d$, defining the bedload-saltation transition for the simulation data. Lines in (b) separate bedload from saltation (dashed line) and bedload and saltation from suspension (dashed-dotted line), as predicted by the simulation version of the cessation threshold model. Note that the simulation data are always nonsuspended (bedload or saltation) because the numerical model neglects turbulent fluctuations around the mean turbulent flow.

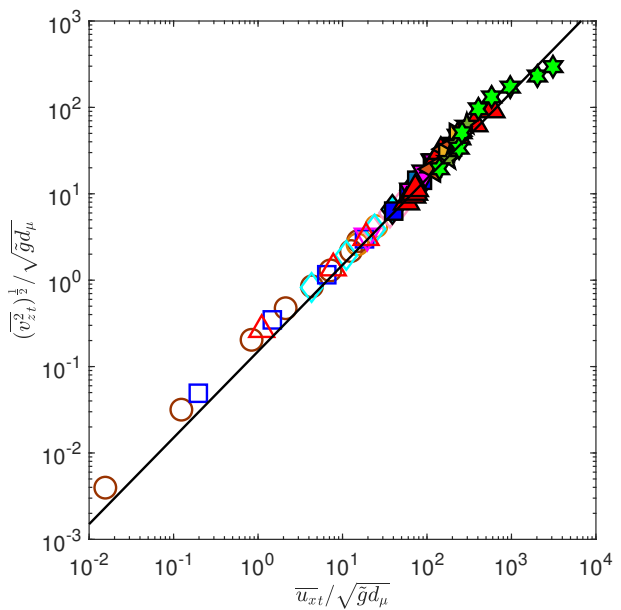


Figure S2: normalized root mean square of the vertical grain velocity $(\bar{v}_{z t}^2)^{1/2} / \sqrt{\tilde{g} d_\mu}$ versus normalized transport layer-averaged flow velocity $\bar{u}_{x t} / \sqrt{\tilde{g} d_\mu}$. Symbols have the same meaning as in Fig. S1. The line indicates proportionality.

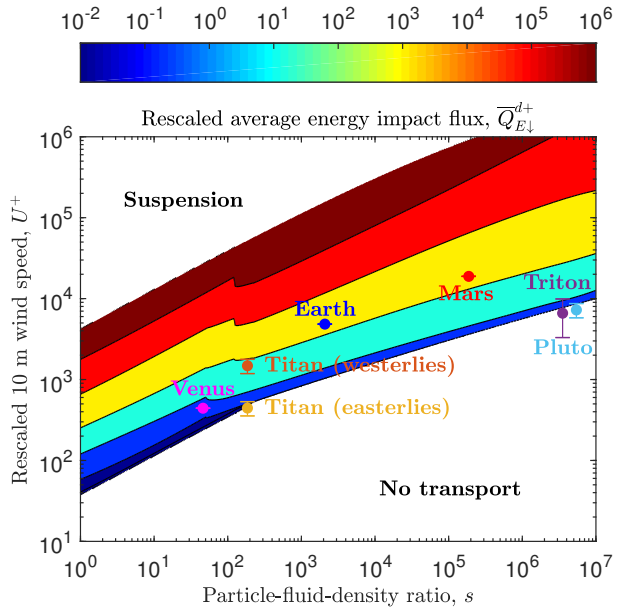


Figure S3: Rescaled average impact flux of the kinetic energy of transported grains $\overline{Q}_{E\downarrow}^{d+} = \overline{Q}_{E\downarrow}^d / [\rho_p(\tilde{g}d_\mu)^{3/2}]$ (color map), where $\overline{Q}_{E\downarrow}^d \equiv \int_{d_1^+}^{d_2^+} Q_{E\downarrow} dd^+ / (d_2^+ - d_1^+)$ (with $Q_{E\downarrow}$ calculated by Eq. (33)), as a function of the rescaled 10 m wind speed $U^+ = U / \sqrt{\tilde{g}d_\mu}$ and density ratio $s \equiv \rho_p / \rho_f$. Symbols and error bars indicate the strongest storms that occur on a given Solar System body over erodible surfaces. $\overline{Q}_{E\downarrow}^{d+}$ represents an estimation for the dust emission potential for saltation conditions.

References

1. M. C. Bourke, *et al.*, *Geomorphology* **121**, 1 (2010).
2. J. F. Kok, E. J. R. Parteli, T. I. Michaels, D. B. Karam, *Reports on Progress in Physics* **75**, 106901 (2012).
3. R. D. Lorenz, *Icarus* **230**, 162 (2014).
4. S. Diniega, *et al.*, *Aeolian Research* **26**, 5 (2017).
5. O. Durán Vinent, B. Andreotti, P. Claudin, C. Winter, *Nature Geoscience* **12**, 345 (2019).
6. C. Sagan, C. Chyba, *Nature* **346**, 546 (1990).
7. M. W. Telfer, *et al.*, *Science* **360**, 992 (2018).
8. P. Jia, B. Andreotti, P. Claudin, *Proceedings of the National Academy of Sciences of the United States of America* **114**, 2509 (2017).
9. D. Berzi, J. T. Jenkins, A. Valance, *Journal of Fluid Mechanics* **786**, 190 (2016).
10. M. Lämmel, K. Kroy, *Physical Review E* **96**, 052906 (2017).
11. P. Claudin, B. Andreotti, *Earth and Planetary Science Letters* **252**, 30 (2006).
12. J. F. Kok, *Geophysical Research Letters* **37**, L12202 (2010).
13. F. Comola, J. Gaume, J. F. Kok, M. Lehning, *Geophysical Research Letters* **46**, 5566 (2019).
14. J. S. Méndez Harper, *et al.*, *Nature Geoscience* **10**, 260 (2017).

15. X. Yu, S. M. Hörst, C. He, P. McGuigan, N. T. Bridges, *Journal of Geophysical Research: Planets* **122**, 2610 (2017).
16. T. Pähzt, *et al.*, *Journal of Geophysical Research: Earth Surface* **126**, e2020JF005859 (2021).
17. T. Pähzt, A. H. Clark, M. Valyraakis, O. Durán, *Reviews of Geophysics* **58**, e2019RG000679 (2020).
18. T. Pähzt, O. Durán, *Journal of Geophysical Research: Earth Surface* **123**, 1638 (2018).
19. T. Pähzt, O. Durán, *Physical Review Letters* **124**, 168001 (2020).
20. T. Pähzt, O. Durán, *Physical Review Fluids* **3**, 104302 (2018).
21. O. Durán, B. Andreotti, P. Claudin, *Physics of Fluids* **24**, 103306 (2012).
22. R. Greeley, B. White, R. Leach, J. Iversen, J. Pollack, *Geophysical Research Letters* **3**, 417 (1976).
23. R. Greeley, R. Leach, B. White, J. Iversen, J. Pollack, *Geophysical Research Letters* **7**, 121 (1980).
24. J. D. Iversen, B. R. White, *Sedimentology* **29**, 111 (1982).
25. R. Greeley, *et al.*, *Icarus* **57**, 112 (1984).
26. D. M. Burr, *et al.*, *Nature* **517**, 60 (2015).
27. D. M. Burr, *et al.*, *Aeolian Research* **45**, 100601 (2020).
28. C. Swann, D. J. Sherman, R. C. Ewing, *Geophysical Research Letters* **47**, e2019GL084484 (2020).

29. B. Andreotti, P. Claudin, J. J. Iversen, J. P. Merrison, K. R. Rasmussen, *Proceedings of the National Academy of Sciences of the United States of America* **118**, e2012386118 (2021).

30. T. Pähzt, M. Valyrakis, X. H. Zhao, Z. S. Li, *Geosciences* **8**, 314 (2018).

31. C. T. Crowe, J. D. Schwarzkopf, M. Sommerfeld, Y. Tsuji, *Multiphase Flows with Droplets and Particles* (Taylor & Francis Group, Boca Raton, 2012).

32. D. Beladjine, M. Ammi, L. Oger, A. Valance, *Physical Review E* **75**, 061305 (2007).

33. R. A. Bagnold, *The Geographical Journal* **89**, 409 (1937).

34. R. L. Martin, J. F. Kok, *Journal of Geophysical Research: Earth Surface* **123**, 1546 (2018).

35. W. Zhu, *et al.*, *Journal of Geophysical Research: Earth Surface* **124**, 2311 (2019).

36. W. S. Chepil, *Soil Science* **60**, 397 (1945).

37. K. Sugiura, K. Nishimura, N. Maeno, T. Kimura, *Cold Regions Science and Technology* **27**, 83 (1998).

38. A. Clifton, J. D. Rüedi, M. Lehning, *Journal of Glaciology* **52**, 585 (2006).

39. M. Creyssels, *et al.*, *Journal of Fluid Mechanics* **625**, 47 (2009).

40. T. D. Ho, A. Valance, P. Dupont, A. Ould El Moctar, *Physical Review Letters* **106**, 094501 (2011).

41. R. L. Martin, J. F. Kok, *Science Advances* **3**, e1602569 (2017).

42. J. L. Ralaiarisoa, *et al.*, *Physical Review Letters* **124**, 198501 (2020).

43. E. Meyer-Peter, R. Müller, *Proceedings of the 2nd Meeting of the International Association for Hydraulic Structures Research* (IAHR, Stockholm, 1948), pp. 39–64.

44. G. M. Smart, M. N. R. Jaeggi, *Mitteilungen der Versuchsanstalt für Wasserbau, Hydrologie und Glaziologie*, no. 64 (ETH Zurich, Zurich, Switzerland, 1983).

45. H. Capart, L. Fraccarollo, *Geophysical Research Letters* **38**, L20402 (2011).

46. M. Wong, G. Parker, *Journal of Hydraulic Engineering* **132**, 1159 (2006).

47. B. Charnay, *et al.*, *Nature Geoscience* **8**, 362 (2015).

48. S. Rodriguez, *et al.*, *Nature Geoscience* **11**, 727 (2018).

49. T. Pähzt, O. Durán, *Physical Review Fluids* **2**, 074303 (2017).

50. O. Durán, B. Andreotti, P. Claudin, *Advances in Geosciences* **37**, 73 (2014).

51. O. Durán, P. Claudin, B. Andreotti, *Proceedings of the National Academy of Sciences of the United States of America* **111**, 15665 (2014).

52. T. D. Ho, Etude expérimentale du transport de particules dans une couche limite turbulente, Ph.D. thesis, University of Rennes, Rennes, France (2012).

53. J. Guo, P. Y. Julien, *The Fifth International Symposium on Environmental Hydraulics (ISEH V)*, 5 (University of Nebraska - Lincoln, Tempe, Arizona, 2007), pp. 1–6.

54. B. Camenen, *Journal of Hydraulic Engineering* **133**, 229 (2007).

55. J. Iversen, R. Greeley, J. R. Marshall, J. B. Pollack, *Sedimentology* **34**, 699 (1987).

56. J. M. Moore, *et al.*, *Icarus* **246**, 65 (2015).

57. R. Sullivan, J. F. Kok, *Journal of Geophysical Research: Planets* **122**, 2111 (2017).

58. K. C. Leonard, L. B. Tremblay, J. E. Thom, D. R. MacAyeal, *Cold Regions Science and Technology* **70**, 71 (2011).

59. N. T. Bridges, *et al.*, *Geology* **40**, 31 (2012).
60. M. M. Baker, *et al.*, *Journal of Geophysical Research: Planets* **123**, 1380 (2018).
61. E. Kaufmann, N. I. Kömle, G. Kargl, *Icarus* **185**, 274 (2006).
62. R. Greeley, R. E. Arvidson, *Earth, Moon, and Planets* **50**, 127 (1990).
63. S. Albugami, S. Palmer, J. Cinnamon, J. Meersmans, *Geosciences* **9**, 162 (2019).
64. R. Sullivan, *et al.*, *Nature* **436**, 58 (2005).
65. A. P. Ingersoll, *Nature* **344**, 315 (1990).
66. F. Forget, *et al.*, *Icarus* **287**, 54 (2017).